Enhanced response of soil respiration to experimental warming upon thermokarst formation

Guanqin Wang [1,2,3,11], Yunfeng Peng [1,2,11], Leiyi Chen [1,2], Benjamin W. Abbott [4], Philippe Ciais [5], Luyao Kang[1,2,3], Yang Liu[1,2,6], Qinlu Li[1,2], Josep Peñuelas [7,8], Shuqi Qin[1,2], Pete Smith [9], Yutong Song[1,2,3], Jens Strauss [10], Jun Wang[1,2], Bin Wei[1,2,3], Jianchun Yu[1,2], Dianye Zhang[1,2] & Yuanhe Yang [1,2,3] ✉

As global temperatures continue to rise, a key uncertainty of terrestrial carbon (C)–climate feedback is the rate of C loss upon abrupt permafrost thaw. This type of thawing—termed thermokarst—may in turn accelerate or dampen the response of microbial degradation of soil organic matter and carbon dioxide (CO_2) release to climate warming. However, such impacts have not yet been explored in experimental studies. Here, by experimentally warming three thermo-erosion gullies in an upland thermokarst site combined with incubating soils from five additional thermokarst-impacted sites on the Tibetan Plateau, we investigate how warming responses of soil CO_2 release would change upon upland thermokarst formation. Our results show that warming-induced increase in soil CO_2 release is ~5.5 times higher in thermokarst features than the adjacent non-thermokarst landforms. This larger warming response is associated with the lower substrate quality and higher abundance of microbial functional genes for recalcitrant C degradation in thermokarst-affected soils. Taken together, our study provides experimental evidence that warming-associated soil CO_2 loss becomes stronger upon abrupt permafrost thaw, which could exacerbate the positive soil C–climate feedback in permafrost-affected regions.

Vast quantities of soil organic carbon (C) are stored in permafrost-affected regions (-1,014–1,672 Pg C; 1 Pg = 10^{15} g)[1–3] where the rate of climate warming is reported to be faster than the global average[4]. This rapid warming and resultant permafrost thaw accelerates the microbial breakdown of soil organic matter (SOM), potentially elevating atmospheric carbon dioxide (CO_2) or methane concentrations and triggering a positive permafrost C–climate feedback[5,6]. However, an intercomparison of permafrost C-enabled models identified diverse projections, ranging from a net C gain to a substantial C loss (−167 to 641 Pg C between 2010 and 2299)[7], partly owing to our poor understanding

¹State Key Laboratory of Vegetation and Environmental Change, Institute of Botany, Chinese Academy of Sciences, Beijing, China. ²China National Botanical Garden, Beijing, China. ³University of Chinese Academy of Sciences, Beijing, China. ⁴Department of Plant and Wildlife Sciences, Brigham Young University, Provo, UT, USA. ⁵Laboratoire des Sciences du Climat et de l'Environnement, LSCE/IPSL, CEA-CNRS-UVSQ, Université Paris-Saclay, Gif-sur-Yvette, France. ⁶College of Resources and Environmental Sciences, Key Laboratory of Farmland Eco-Environment of Hebei, Hebei Agricultural University, Baoding, China. ⁷CSIC, Global Ecology Unit CREAF-CSIC-UAB, Barcelona, Spain. ⁸CREAF, Cerdanyola del Vallès, Spain. ⁹Institute of Biological and Environmental Sciences, University of Aberdeen, Aberdeen, UK. ¹⁰Permafrost Research Section, Alfred Wegener Institute, Helmholtz Centre for Polar and Marine Research, Potsdam, Germany. ¹¹These authors contributed equally: Guanqin Wang, Yunfeng Peng. ✉e-mail: yhyang@ibcas.ac.cn

about the responses of the ecosystem C cycle to abrupt permafrost thaw, termed thermokarst[8]. Thermokarst occurs owing to the melting of ice-rich permafrost, which can alter the trajectory of the permafrost C cycle[9]. Given that ongoing climate warming would affect many ecosystem processes in both thermokarst and non-thermokarst areas, an interesting question is whether warming effects on soil CO_2 flux could differ between these two distinct landforms. If warming effects are amplified upon thermokarst formation, the positive permafrost C–climate feedback will be intensified. It is thus imperative to test whether the warming response of soil CO_2 release will become stronger where thermokarst landscape occurs.

Among the generally identified thermokarst landforms (lake, wetland and upland thermokarst), upland thermokarst (estimate of 0.91×10^6 km^2) often occurs on moderate slopes or along water courses[8,9]. Upland thermokarst formation can restructure land surface morphology, causing abrupt changes in soil environments, organic matter composition and microbial properties[10,11]. For example, observational studies demonstrate a substantial decline in soil organic C quality[12] and soil microbial diversity[11,13] following upland permafrost collapse. These changes could not only alter the rate of soil-respired CO_2 (refs. 8,14), but also affect its response to the ongoing warming. On the one hand, compared with the high-quality soil substrates, low-quality soil substrates in the collapsed area require higher activation energy to be decomposed[15,16], and their decomposition is thus more sensitive to elevated temperature. On the other hand, thermokarst-induced decrease in microbial diversity[11] probably exerts dual effects on the temperature response of SOM decomposition: the reduction of microbial diversity may lead to a decline in warming effect because of the reduced microbial metabolic potential[17], but it may also elevate the warming effect because higher biodiversity is associated with greater functional resistance[18,19], and thus the declined microbial diversity would render microbial mediated functions (for example, SOM decomposition) more sensitive to environmental change, such as climate warming. However, current in situ warming experiments have all been conducted in non-thermokarst landscapes[20–22]. Whether and how warming effects on soil CO_2 fluxes would change upon thermokarst formation, to date, has never been explicitly explored in any experimental studies in permafrost areas.

Here we identified three thermo-erosion gullies at a large thermokarst feature in Shaliuhe on the northeastern Tibetan Plateau (37° 28′ N, 100° 17′ E, ~3,900 m above sea level; Extended Data Fig. 1a), which has the largest distribution of alpine permafrost on Earth and stores a large amount of C (~15.3 –46.2 Pg C at a depth of 3 m; refs. 23,24). In each gully, we conducted in situ warming experiments inside (collapsed area) and outside the gully (non-collapsed area) using open-top chambers (OTCs; Extended Data Fig. 2). Based on these well-replicated warming experiments, we compared warming effects on soil CO_2 flux (hereafter soil respiration; Rs) between collapsed and non-collapsed areas. To verify the broader representativeness of single-site findings, we collected soils from the Shaliuhe site and five additional upland thermokarst-impacted sites (Extended Data Fig. 1 and Supplementary Table 1) to examine how temperature sensitivity of CO_2 release (the factor by which respiration rises as a result of a 10 °C increase, Q_{10}) responds to permafrost collapse using a laboratory incubation experiment. Further, based on in situ warming experiments, combining soil physiochemical analyses, solid-state ^{13}C nuclear magnetic resonance[25] and metagenomic sequencing[26], we explored the associations of Rs response with various biotic and abiotic variables to identify the key factors that were most strongly correlated with the differences in warming effects.

Intensified Rs response to warming in thermokarst area

In the field experiments, we simultaneously measured Rs and its heterotrophic component, soil temperature and moisture three times per month during the growing season in 2019 and 2020. Rs and its
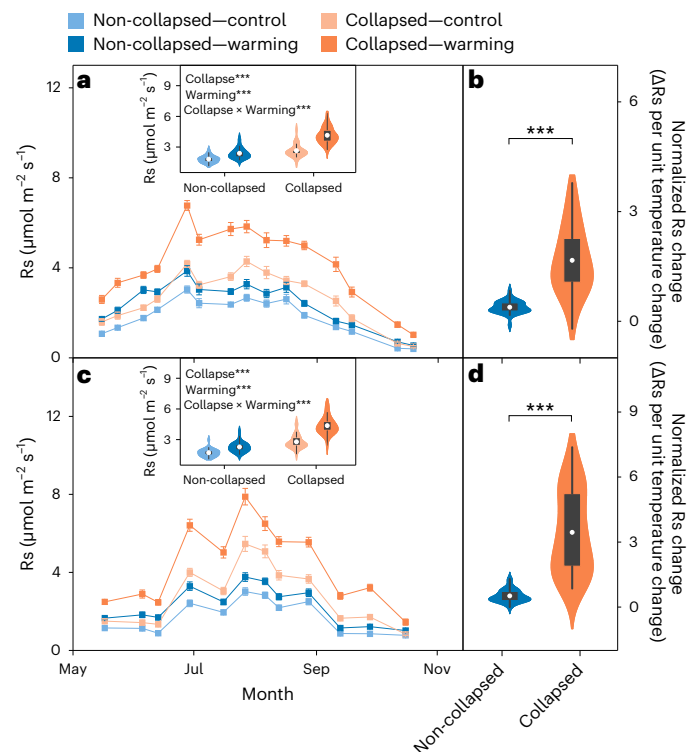

Fig. 1 | Response of Rs to permafrost collapse and experimental warming at the Shaliuhe site. a,c, Seasonal dynamics and averages of Rs during the growing seasons in 2019 (**a**) and 2020 (**c**). Data are presented with mean values ± s.e.m. (n = 30). Inserts show effects of permafrost collapse, experimental warming and their interactions on seasonal averages of Rs. **b,d,** Normalized Rs change in 2019 (**b**) and 2020 (**d**). The ends of the boxes represent the 25th and 75th percentiles, and the whiskers refer to the 10th and 90th quartiles. The white dot in each box shows the average (n = 30). These comparisons were analysed based on linear mixed-effects models with one-sided F tests. ***P < 0.001.

heterotrophic component were separated by soil collars with different lengths (that is, the 5-cm-long and 42-cm-long collars for measuring Rs and heterotrophic respiration (Rh), respectively)[27,28]. Given that Rh measurement would create an artificial situation without root exudates in deep collars (see Methods for details), the measured Rh is not the actual Rh, but a potential Rh under our specific experimental conditions (hereafter referred to as Rhp). The two consecutive years' measurements revealed that both Rs and Rhp displayed hump-shaped trends over the growing season regardless of treatments (Fig. 1a,c and Extended Data Fig. 3a,c), with the Rhp contributing to a major portion of Rs (~67%; Supplementary Fig. 1). Considering the above-mentioned methodological limitation of Rhp and its major contribution to Rs, our following analyses concentrated on Rs while the Rhp data were only used to supplement the Rs results. We showed that, in unwarmed plots, the Rs significantly increased by an average of 55.4 ± 8.0% (mean ± s.e.m.) upon permafrost collapse (Fig. 1). The higher Rs upon thermokarst formation may be explained by the following reasons: (1) after permafrost collapse, the increase in soil permeability and thinning of the diffusive boundary layer[29] would open up previously obstructed vertical and lateral flow paths and thereby enhance transportation of organic matter, which favours microbial CO_2 emission[29,30]; (2) the above environmental changes and decrease in volumetric soil moisture (from 57.1 ± 0.4% to 51.5 ± 0.7%; Extended Data Fig. 4c,d) would also allow more oxygen to fill the voids of the organic layer, thus exacerbating the SOM decomposition[29,30]; and (3) permafrost collapse would disrupt soil aggregates[31], weakening SOM stability and then accelerating SOM decomposition[32]. Overall, these changes would lead to the higher Rs upon permafrost collapse observed in this study.

The OTC deployment increased soil temperature in the upper 10 cm by an average of 1.3 °C (from 6.0 to 7.3 °C) across the thermokarst landforms (non-collapsed and collapsed areas) and growing seasons (2019 and 2020; Extended Data Fig. 4a,b). However, volumetric soil moisture at various depths was insensitive to experimental warming (control versus warming: 55.4 versus 57.8%, 61.3 versus 63.4% and 56.1 versus 51.4% across non-collapsed and collapsed areas at 10, 20 and 30 cm depth, respectively; Extended Data Fig. 5d–f). Warming treatment substantially increased Rs by an average of 45.6 ± 1.8%, which should mostly result from the top 10 cm soil due to the limited warming effects in deeper soils (Extended Data Fig. 5a–c). By taking advantage of the simultaneously measured Rs in warmed and control plots between the collapsed and non-collapsed areas, we explored whether and how warming effects would change upon thermokarst formation. To this end, we first computed the normalized Rs response because the rising magnitude of topsoil (0–10 cm) temperature by OTC differed between the two land features, as indicated by the significant interaction between permafrost collapse and experimental warming (Extended Data Fig. 4a,b). The normalized warming effects were calculated using the following formula[33]:

$$\text{Normalized Rs change} = \frac{\text{Rs}_{\text{Warming}} - \text{Rs}_{\text{Control}}}{T_{\text{Warming}} - T_{\text{Control}}} \quad (1)$$

where $\text{Rs}_{\text{Warming}}$ and $\text{Rs}_{\text{Control}}$ are Rs (μmol m^{-2} s^{-1}) in warmed and control plots, respectively, and T_{Warming} and T_{Control} are the topsoil temperatures (°C) in warmed and control plots, respectively. After normalization, we found that the Rs response was much stronger upon thermokarst formation (increased 4.2- and 6.7-fold in 2019 and 2020, respectively, both $P < 0.001$; Fig. 1b,d). To further validate these results, we estimated the apparent Q_{10} of Rs by fitting Rs with the corresponding topsoil temperature in unwarmed plots using an exponential function[27] (see Supplementary Note 1 for detailed calculations). Results showed that the apparent Q_{10} was significantly higher upon permafrost collapse (Extended Data Fig. 6a,b), supporting the results from the in situ warming experiments. Notably, similar patterns of the normalized warming effects (Extended Data Fig. 3) and the apparent Q_{10} (Extended Data Fig. 6c,d) were observed for Rhp, providing additional evidence for a stronger soil CO_2 response to experimental warming in thermokarst landscapes.

To test the universality of the single-site findings, we collected soil samples from five additional thermo-erosion gullies across a 550 km permafrost transect on the Tibetan Plateau (Extended Data Fig. 1). We then conducted a laboratory incubation using soils from the three gullies at the Shaliuhe site plus five additional gullies from Ebo, Mole, Reshui, Huashixia and Huanghe sites. The Q_{10} was calculated from the soil CO_2 release rate at two incubation temperatures[34] (5 °C and 15 °C; Methods). During most of the measurement occasions and throughout the incubation period, significant increases in Q_{10} values were observed in collapsed relative to non-collapsed areas (ranging from 12% to 53%) at all sites except for Huashixia (Fig. 2 and Extended Data Fig. 7). Although we observed a consistent response of warming-induced soil CO_2 release to thermokarst formation both in field and laboratory experiments, the field-based Q_{10} values (non-collapsed versus collapsed: 5.1 ± 0.1 versus 7.2 ± 0.1; Extended Data Fig. 6) were much higher than those from the laboratory incubation (non-collapsed versus collapsed: 2.2 ± 0.1 versus 2.7 ± 0.2; Fig. 2). Such a difference is probably induced by methodological discrepancy. For the incubation experiment, temperature is the major factor linked to changes in soil CO_2 emissions. While in the field, other factors may covary (for example, elevated substrate availability and microbial biomass) with temperature increase over the growing season[29], which could then interact with temperature to promote Rs and yield larger apparent Q_{10} values (see Supplementary Note 2 for detailed discussions).
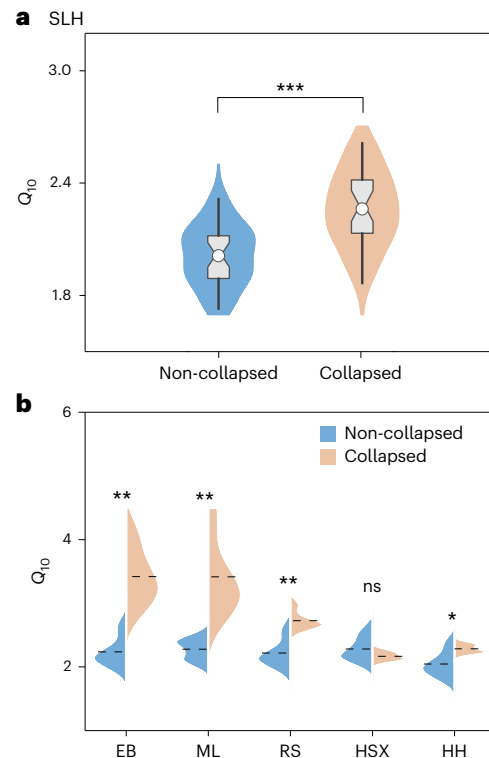

Fig. 2 | Difference in Q_{10} between collapsed and non-collapsed areas for the six thermokarst-affected sites. a, Q_{10} between collapsed and non-collapsed areas for the Shaliuhe site (SLH). Samples ($n = 30$) were collected from three thermo-erosion gullies in 2020. The ends of the boxes represent the 25th and 75th percentiles, and the whiskers represent the 10th and 90th quartiles. The white dot in each box represents the average. **b**, Q_{10} between collapsed and non-collapsed areas for the five additional sites. Samples ($n = 5$) were collected in 2020. The dashed lines denote the average. EB, Ebo site; ML, Mole site; RS, Reshui site; HSX, Huashixia site; HH, Huanghe site. These comparisons were analysed based on linear mixed-effects models with one-sided F tests. ns, non-significant; $*P < 0.05$; $**P < 0.01$; $***P < 0.001$.

Rs response associated with SOM quality and microbial genes

The stronger response of Rs upon thermokarst formation may be associated with many biotic and abiotic factors, such as plant, edaphic and microbial properties, and so on. To identify the key factors that were most strongly correlated with the different warming effects on Rs, we measured a number of potential factors and compared their differences between collapsed and non-collapsed areas. Specifically, we first compared plant attributes and observed that these variables remained stable upon permafrost collapse (Supplementary Fig. 2a–d), indicating that the warming responses of Rs may be minimally related to plant attributes. We then explored changes in soil characteristics and microbial properties, and found that there were significant changes in these variables (Fig. 3a–i, Extended Data Figs. 8 and 9, and Supplementary Figs. 2–4; see Supplementary Note 3 for detailed descriptions). Finally, based on the above comparisons together with the single variable relationships between Rs response and these factors, we constructed the structural equation modelling (SEM) to tease apart the pathways and relative importance of edaphic and microbial factors (Fig. 3j and Supplementary Figs. 2q and 5). The SEM analysis revealed that the normalized Rs change was directly linked to substrate quality and the abundances of microbial functional genes (Fig. 4a), with the standardized path coefficients of 0.31 and 0.29, respectively (Fig. 4b). In addition, soil moisture and clay+silt were indirectly correlated with the normalized Rs change via substrate quality and the abundances of microbial functional genes (Fig. 4a). Similar results were also found
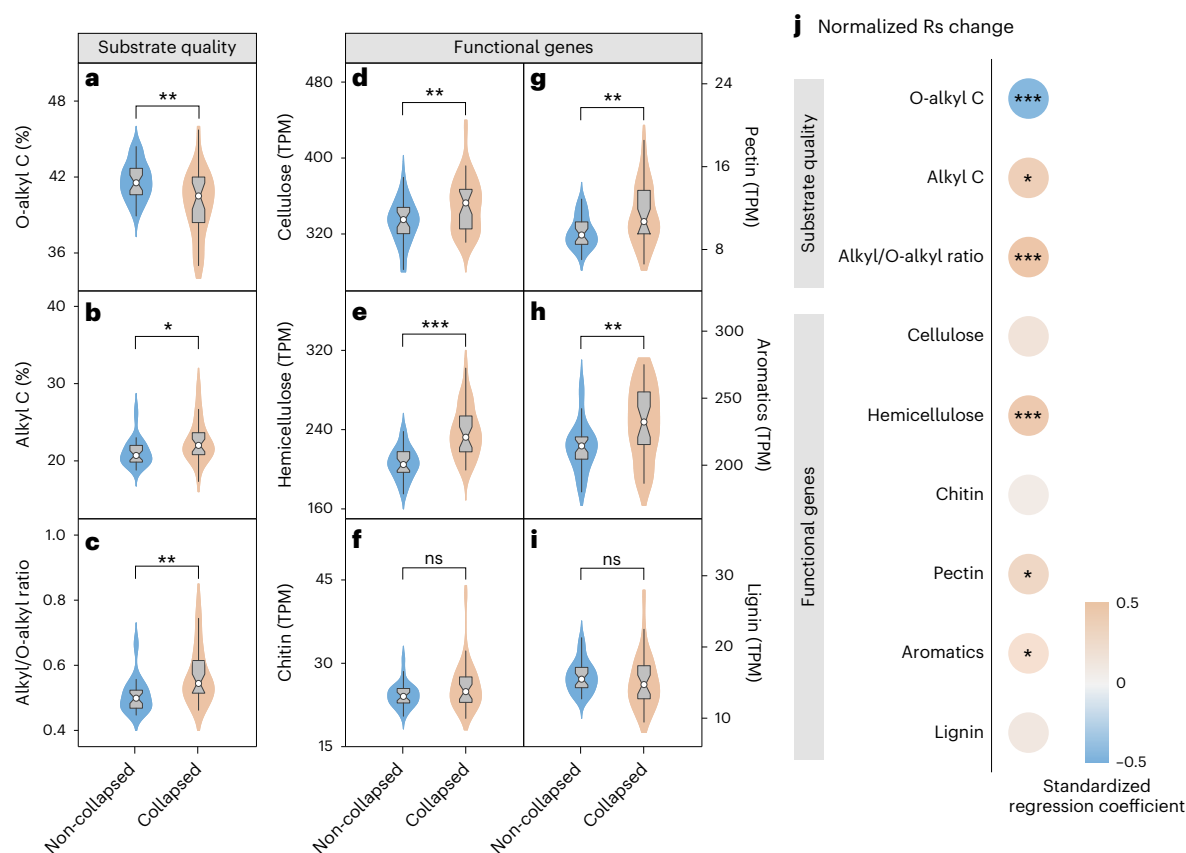
Fig. 3 | Changes in substrate quality and microbial functional gene abundances upon permafrost collapse and their relationships with the normalized Rs change. a–i, Changes in O-alkyl C (**a**), alkyl C (**b**), alkyl/O-alkyl ratio (**c**) and the relative abundances of C degradation genes as transcripts per million reads mapped (TPM) upon thermokarst formation for cellulose (**d**), hemicellulose (**e**), chitin (**f**), pectin (**g**), aromatics (**h**) and lignin (**i**). The ends of the boxes represent the 25th and 75th percentiles, and the whiskers represent the 10th and 90th quartiles. The white dot in each box represents the average (n = 30). **j,** Standardized regression coefficient of the relationships of normalized Rs change with substrate quality and the abundances of microbial functional genes. The colour scale indicates the strength and sign of the correlations. Samples were collected from three thermo-erosion gullies at the Shaliuhe site in 2019. These comparisons were analysed based on linear mixed-effects models with one-sided F tests. ns, non-significant; *P < 0.05; **P < 0.01; ***P < 0.001.

for Rhp response (Extended Data Fig. 10). These results highlighted that substrate quality and microbial functional genes were probably the key factors related to the differences in warming effects between collapsed and non-collapsed areas.

While the statistical correlations may not infer the cause–effect relationships, the results allow for a causal speculation on these associations by prior ecological principles. We observed a positive correlation between normalized Rs change and substrate quality (Fig. 3j). In our study site, the recalcitrant C components were found to increase upon thermokarst formation (Fig. 3b). In such a case, we may expect that, based on the 'C quality–temperature' hypothesis[15,35], the SOM decomposition is more responsive to experimental warming in collapsed than that in non-collapsed areas because the decomposition of recalcitrant substrates requires higher activation energy, which is therefore more sensitive to warming[35]. Then an interesting question is why there was an increase in the recalcitrant C components. Such a change may be explained by the preferential usage of the labile C by microbial decomposition and hydrologic transport/lateral flux[12,36]. On the one hand, the easily degradable compounds can be rapidly accessed by soil microorganisms after permafrost collapse[37,38], while the more recalcitrant alkyl C would accumulate and eventually become more abundant within soils of collapsed vegetation patches[12]. On the other hand, the weakened mineral absorption (as indicated by reduced clay+silt content) and increased hydrological transport in collapsed soils (as reflected by reduced soil moisture; Fig. 4a) may lead to the leaching of labile SOM[39], while the recalcitrant compounds are more readily adsorbed to the leftover mineral soils[40], thus reducing the SOM quality.

Although there were no obvious relationships between soil CO$_2$ flux response and bacterial diversity changes (Extended Data Fig. 9a,b), the normalized Rs change was positively correlated with abundances of microbial functional genes involved in SOM decomposition (Fig. 4), particularly those involved in recalcitrant substrate decomposition (that is, those C degradation genes for pectin and aromatic compounds; Fig. 3j). Increases in microbial functional genes were associated with reduced soil moisture and clay+silt content upon permafrost collapse (Fig. 4a), which allowed more oxygen as for a greater microbial functioning. The increased abundance of these functional genes after thermokarst formation implies an elevated potential for the decomposition of recalcitrant SOM[11,41], which may enhance the Rs response at higher temperatures based on the 'C quality–temperature' hypothesis[15,35]. We also found a pronounced increase in the normalized response of oxidase activity in the collapsed soils (Extended Data Fig. 8), implying an enhanced degradation of recalcitrant SOM and further supporting the higher warming response of Rs upon thermokarst formation.

Apart from the above pathways supported by our statistical results, there may be other processes underlying the different warming effects that were not measured or excluded from the SEM analysis, such as physiochemical protection and other environmental changes. First, the larger Rs response may be associated with destabilized aggregate protection. Permafrost collapse as a disturbance together with the decreased clay+silt (Supplementary Fig. 2i) is supposed to weaken physical occlusion within aggregates[31] and thus increase substrate accessibility, which would then alleviate constraints to
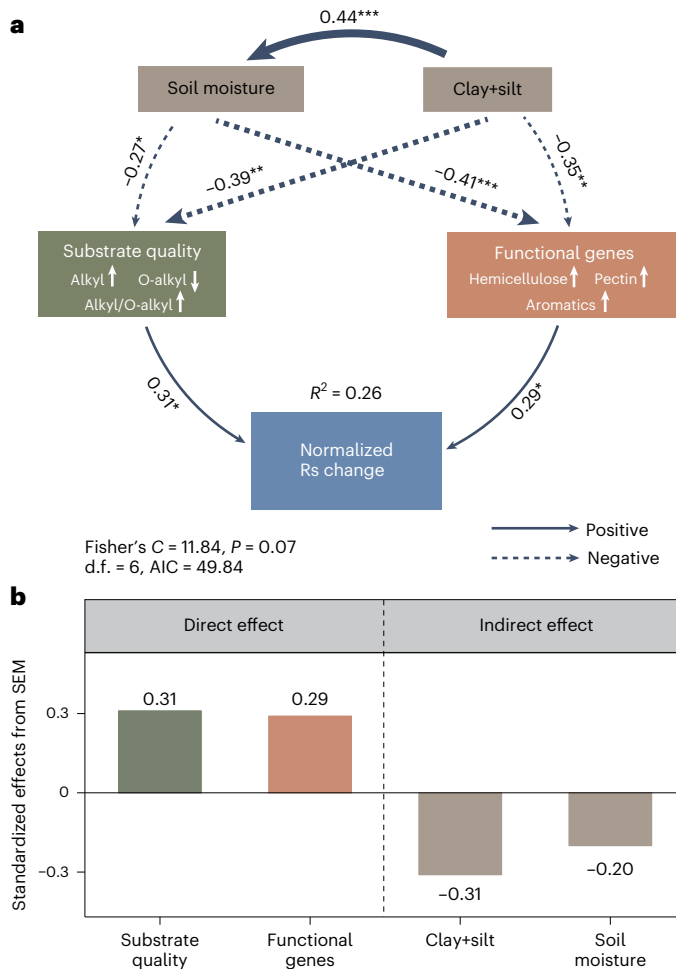
a

b

Fig. 4 | Effects of abiotic and biotic factors on the normalized Rs change.
a, SEM of the direct and indirect pathways that link to the normalized Rs change. Solid and dotted arrows represent positive and negative relationships, respectively. Arrow width is proportional to the strength of the relationship. The numbers adjacent to the arrows denote standardized path coefficients. Substrate quality is the first component from the PCA of the variables listed inside the rectangles, with ↑ and ↓ indicating positive and negative correlations between the factors and the first component, respectively. Microbial functional genes represent the weighted average of the first and second components from the PCA of the variables inside the rectangle, with ↑ indicating a positive correlation between the factors and the weighted average of the first and second components. *$P < 0.05$; **$P < 0.01$; ***$P < 0.001$; AIC, Akaike information criterion. **b**, Standardized direct effects of substrate quality, abundance of microbial functional genes and indirect effects of edaphic variables (clay+silt and soil moisture) on the normalized Rs change.

microbial decomposition and further favour larger warming response of Rs. Despite the vital role of reactive minerals in attenuating the temperature response of microbial decomposition[35], it might be less important in our study because organically complexed Fe increased upon permafrost collapse (Supplementary Fig. 2l), which would attenuate Rs response from the theoretical perspective but contrasted from the stronger response detected here. Second, the larger Rs response may also be related to interaction effects of temperature with other environmental changes. Following permafrost collapse, decrease in soil moisture (Extended Data Fig. 4c,d) and associated increase in soil permeability[42] and thinning of the diffusive boundary layer[43] would allow as much as substrates and oxygen for microbial assess. The enhanced supplies of substrates and oxygen would then amplify the temperature effect on soil CO_2 flux, favouring stronger normalized Rs response. In support of this argument, the observed difference of Q_{10}

between collapsed and non-collapsed areas was smaller in laboratory incubation compared with that in the field (0.5 ± 0.2 versus 2.1 ± 0.2; Fig. 2 and Extended Data Fig. 6a,b), indicating that the interaction effects would amplify the Rs response detected in situ.

Implications for soil CO_2 release under climate warming

By experimentally warming three thermo-erosion gullies in an upland thermokarst site combined with incubating soils from another five thermokarst-impacted sites on the Tibetan Plateau, this study provided multiple lines of evidence that the warming-associated soil CO_2 loss became stronger under upland thermokarst formation. In such a case, thermokarst-affected soils were estimated to respire an additional 422 ± 51 g C m^{-2} yr^{-1} compared with the non-thermokarst landforms under a 2 °C warming (the warming magnitude in permafrost regions by the end of the twenty-first century under a moderate scenario[44]). As a preliminary exploration of global importance, we extrapolated the warming response of Rs to all upland thermokarst regions in the Northern Hemisphere (0.91×10^6 km^2)[9] and found 0.4 ± 0.05 Pg C yr^{-1} of the additional soil CO_2 loss (see Supplementary Note 4 and Supplementary Fig. 6 for detailed calculations). This warming-induced additional CO_2 release upon thermokarst formation corresponds to roughly a quarter of the projected permafrost soil CO_2 losses (2 Pg C yr^{-1}) by the end of the twenty-first century[45]. Our estimate indeed has uncertainties owing to methodological limitations. For instance, the OTC warming method would cause artefact chamber effects that are not associated with warming (for example, local wind shielding, rainfall interception and so on)[46], which may lead to an overstatement of the warming effects and thus bias of the estimated additional CO_2 emission (see Supplementary Note 4 for details); the spatial heterogeneity of climate, vegetation and soil properties may also influence the Rs responses and lead to uncertainties of the global extrapolation. Despite this, our findings highlight that the intensified warming response of soil CO_2 efflux upon thermokarst formation cannot be neglected when projecting the future trajectory of permafrost C–climate feedback. More broadly, our findings may be extrapolated to other disturbed versus non-disturbed sites, where disturbances such as tillage[47] and fire[48] led to the loss of labile compounds, while soil erosion[49], deforestation and land use change[50] altered community composition. Consequently, the strength of soil CO_2 release may be underestimated if the permafrost collapse and other analogous disturbances are ignored. Extending studies that focus on warming effects simultaneously in disturbed versus non-disturbed sites are thus required to be performed in diverse regions and ecosystems for a more accurate estimation of the soil-respired CO_2 under future warming.

Online content

Any methods, additional references, Nature Portfolio reporting summaries, source data, extended data, supplementary information, acknowledgements, peer review information; details of author contributions and competing interests; and statements of data and code availability are available at https://doi.org/10.1038/s41561-024-01440-2.

References

1. Mishra, U. et al. Spatial heterogeneity and environmental predictors of permafrost region soil organic carbon stocks. *Sci. Adv.* **7**, eaaz5236 (2021).
2. Tarnocai, C. et al. Soil organic carbon pools in the northern circumpolar permafrost region. *Glob. Biogeochem. Cycles* **23**, GB2023 (2009).
3. Hugelius, G. et al. Estimated stocks of circumpolar permafrost carbon with quantified uncertainty ranges and identified data gaps. *Biogeosciences* **11**, 6573–6593 (2014).
4. IPCC *Climate Change 2023: Synthesis Report* (eds Core Writing Team, Lee, H. & Romero, J.) (Cambridge Univ. Press, 2023).

5. Schuur, E. A. G. et al. Permafrost and climate change: carbon cycle feedbacks from the warming Arctic. *Annu. Rev. Environ. Resour.* **47**, 343–371 (2022).

6. Miner, K. R. et al. Permafrost carbon emissions in a changing Arctic. *Nat. Rev. Earth Environ.* **3**, 55–67 (2022).

7. McGuire, A. D. et al. Dependence of the evolution of carbon dynamics in the northern permafrost region on the trajectory of climate change. *Proc. Natl Acad. Sci. USA* **115**, 3882–3887 (2018).

8. Turetsky, M. R. et al. Carbon release through abrupt permafrost thaw. *Nat. Geosci.* **13**, 138–143 (2020).

9. Olefeldt, D. et al. Circumpolar distribution and carbon storage of thermokarst landscapes. *Nat. Commun.* **7**, 13043 (2016).

10. Harms, T. K., Abbott, B. W. & Jones, J. B. Thermo-erosion gullies increase nitrogen available for hydrologic export. *Biogeochemistry* **117**, 299–311 (2013).

11. Liu, F. et al. Altered microbial structure and function after thermokarst formation. *Glob. Change Biol.* **27**, 823–835 (2021).

12. Liu, F. et al. Reduced quantity and quality of SOM along a thaw sequence on the Tibetan Plateau. *Environ. Res. Lett.* **13**, 104017 (2018).

13. Wang, G. et al. Divergent trajectory of soil autotrophic and heterotrophic respiration upon permafrost thaw. *Environ. Sci. Technol.* **56**, 10483–10493 (2022).

14. Abbott, B. W. & Jones, J. B. Permafrost collapse alters soil carbon stocks, respiration, CH_4, and N_2O in upland tundra. *Glob. Change Biol.* **21**, 4570–4587 (2015).

15. Bosatta, E. & Ågren, G. I. Soil organic matter quality interpreted thermodynamically. *Soil Biol. Biochem.* **31**, 1889–1891 (1999).

16. Craine, J. M., Fierer, N. & McLauchlan, K. K. Widespread coupling between the rate and temperature sensitivity of organic matter decay. *Nat. Geosci.* **3**, 854–857 (2010).

17. Maron, P. et al. High microbial diversity promotes soil ecosystem functioning. *Appl. Environ. Microbiol.* **84**, e02738-17 (2018).

18. Isbell, F. et al. Biodiversity increases the resistance of ecosystem productivity to climate extremes. *Nature* **526**, 574–577 (2015).

19. García, F. C., Bestion, E., Warfield, R. & Yvon-Durocher, G. Changes in temperature alter the relationship between biodiversity and ecosystem functioning. *Proc. Natl Acad. Sci. USA* **115**, 10989–10994 (2018).

20. Hicks Pries, C. E., Schuur, E. A. G., Natali, S. M. & Crummer, K. G. Old soil carbon losses increase with ecosystem respiration in experimentally thawed tundra. *Nat. Clim. Change* **6**, 214–218 (2015).

21. Lupascu, M. et al. High Arctic wetting reduces permafrost carbon feedbacks to climate warming. *Nat. Clim. Change* **4**, 51–55 (2013).

22. Li, F. et al. Warming alters surface soil organic matter composition despite unchanged carbon stocks in a Tibetan permafrost ecosystem. *Funct. Ecol.* **34**, 911–922 (2020).

23. Ding, J. et al. The permafrost carbon inventory on the Tibetan Plateau: a new evaluation using deep sediment cores. *Glob. Change Biol.* **22**, 2688–2701 (2016).

24. Wang, D. et al. A 1km resolution soil organic carbon dataset for frozen ground in the Third Pole. *Earth Syst. Sci. Data* **13**, 3453–3465 (2021).

25. Simpson, M. J. & Simpson, A. J. The chemical ecology of soil organic matter molecular constituents. *J. Chem. Ecol.* **38**, 768–784 (2012).

26. Woodcroft, B. J. et al. Genome-centric view of carbon processing in thawing permafrost. *Nature* **560**, 49–54 (2018).

27. Luo, Y., Wan, S., Hui, D. & Wallace, L. L. Acclimatization of soil respiration to warming in a tall grass prairie. *Nature* **413**, 622–625 (2001).

28. Nottingham, A. T., Meir, P., Velasquez, E. & Turner, B. L. Soil carbon loss by experimental warming in a tropical forest. *Nature* **584**, 234–237 (2020).

29. Davidson, E. A., Janssens, I. A. & Luo, Y. On the variability of respiration in terrestrial ecosystems: moving beyond Q_{10}. *Glob. Change Biol.* **12**, 154–164 (2006).

30. Walvoord, M. A. & Kurylyk, B. L. Hydrologic impacts of thawing permafrost—a review. *Vadose Zone J.* https://doi.org/10.2136/vzj2016.01.0010 (2016).

31. Bailey, V. L., Pries, C. H. & Lajtha, K. What do we know about soil carbon destabilization? *Environ. Res. Lett.* **14**, 083004 (2019).

32. Lehmann, J. & Kleber, M. The contentious nature of soil organic matter. *Nature* **528**, 60–68 (2015).

33. Wang, X. et al. Soil respiration under climate warming: differential response of heterotrophic and autotrophic respiration. *Glob. Change Biol.* **20**, 3229–3237 (2014).

34. Conant, R. T. et al. Sensitivity of organic matter decomposition to warming varies with its quality. *Glob. Change Biol.* **14**, 868–877 (2008).

35. Davidson, E. A. & Janssens, I. A. Temperature sensitivity of soil carbon decomposition and feedbacks to climate change. *Nature* **440**, 165–173 (2006).

36. Pautler, B. G., Simpson, A. J., McNally, D. J., Lamoureux, S. F. & Simpson, M. J. Arctic permafrost active layer detachments stimulate microbial activity and degradation of soil organic matter. *Environ. Sci. Technol.* **44**, 4076–4082 (2010).

37. Mueller, C. W. et al. Large amounts of labile organic carbon in permafrost soils of northern Alaska. *Glob. Change Biol.* **21**, 2804–2817 (2015).

38. Hodgkins, S. B. et al. Changes in peat chemistry associated with permafrost thaw increase greenhouse gas production. *Proc. Natl Acad. Sci. USA* **111**, 5819–5824 (2014).

39. Abbott, B. W., Larouche, J. R., Jones, J. B., Bowden, W. B. & Balser, A. W. Elevated dissolved organic carbon biodegradability from thawing and collapsing permafrost. *J. Geophys. Res. Biogeosci.* **119**, 2049–2063 (2014).

40. Kawahigashi, M., Kaiser, K., Rodionov, A. & Guggenberger, G. Sorption of dissolved organic matter by mineral soils of the Siberian forest tundra. *Glob. Change Biol.* **12**, 1868–1877 (2006).

41. Chen, Y. et al. Large-scale evidence for microbial response and associated carbon release after permafrost thaw. *Glob. Change Biol.* **27**, 3218–3229 (2021).

42. Rowland, J. C. et al. Arctic landscapes in transition: responses to thawing permafrost. *Eos* **91**, 229–230 (2010).

43. Glud, R. N., Berg, P., Fossing, H. & Jørgensen, B. B. Effect of the diffusive boundary layer on benthic mineralization and O_2 distribution: a theoretical model analysis. *Limnol. Oceanogr.* **52**, 547–557 (2007).

44. Soong, J. L., Phillips, C. L., Ledna, C., Koven, C. D. & Torn, M. S. CMIP5 models predict rapid and deep soil warming over the 21st century. *J. Geophys. Res. Biogeosci.* **125**, e2019JG005266 (2020).

45. Schneider von Deimling, T. et al. Estimating the near-surface permafrost-carbon feedback on global warming. *Biogeosciences* **9**, 649–665 (2012).

46. Hollister, R. D. et al. A review of open top chamber (OTC) performance across the ITEX network. *Arct. Sci.* **9**, 331–344 (2023).

47. Cookson, W. R., Murphy, D. V. & Roper, M. M. Characterizing the relationships between soil organic matter components and microbial function and composition along a tillage disturbance gradient. *Soil Biol. Biochem.* **40**, 763–777 (2008).

48. Miesel, J. R., Hockaday, W. C., Kolka, R. K. & Townsend, P. A. Soil organic matter composition and quality across fire severity gradients in coniferous and deciduous forests of the southern boreal region. *J. Geophys. Res. Biogeosci.* **120**, 1124–1141 (2015).

49. Qiu, L. et al. Erosion reduces soil microbial diversity, network complexity and multifunctionality. *ISME J.* **15**, 2474–2489 (2021).

50. Melo, V. F. et al. Soil bacterial diversities and response to deforestation, land use and burning in north Amazon, Brazil. *Appl. Soil Ecol.* **158**, 103775 (2021).

Methods

Site description

Climate warming has intensified thermokarst formation on the Tibetan Plateau[51]. The area affected by thermokarst formation has increased 40-fold during the past five decades[52]. To explore how warming responses of soil CO_2 release will change upon upland thermokarst formation, we established an in situ warming experiment at an upland thermokarst site and incubated soils from five additional thermokarst-impacted sites across a permafrost transect of 550 km (Extended Data Fig. 1). The elevation of the six study sites ranged from 3,515 to 4,707 m above sea level. The mean annual temperature and precipitation varied from −3.1 to 2.6 °C and from 353 to 436 mm, respectively. All sites were characterized as swamp meadows dominated by sedges including *Kobresia tibetica*, *Kobresia royleana* and *Carex atrofuscoides*. The soils were classified as cryosols based on the World Reference Base for Soil Resources[53]. All sites were located in discontinuous permafrost zones, with the active layer thickness being ~0.7–1.1 m. There was no obvious sign of cryoturbation in the six selected sites. See Supplementary Table 1 for detailed information.

Among the six study sites, we selected three thermo-erosion gullies at the Shaliuhe site (Extended Data Fig. 2) and set up the warming experiments in collapsed and non-collapsed areas for each thermo-erosion gully. In the field warming experiments, we measured a series of biotic and abiotic factors such as vegetation and microbial properties, soil physicochemical properties, and substrate quality. To evaluate the generalizability of the response pattern obtained from the field warming experiments, we conducted laboratory incubations using soil samples collected from the Shaliuhe and five additional thermokarst-impacted sites. The specific methods are described below.

In situ warming experiment

Experimental design. The field warming experiment was established during 2017–2018 at the Shaliuhe site (37° 28′ N, 100° 17′ E). The location is ~30 km away from Gangca County, Qinghai Province, China (Extended Data Fig. 1a). The site has a large SOC density (C amount per area; Supplementary Fig. 7), which is much higher than the average on the Tibetan Plateau[54]. We identified three thermo-erosion gullies at a large thermokarst feature on a hillslope with a gentle south-facing incline of 9° (ref. 55). The three gullies were approximately 100 m from each other. A 20 × 20 m² fenced area was set in a relatively flat area at the end of each gully. Meanwhile, an area of the same size was set in the adjacent non-collapsed grassland (Extended Data Fig. 2). Ten 2 × 2 m² blocks were randomly arranged in each enclosure, and two plots within each block were randomly assigned to control and warming treatments. An OTC was employed to warm the near-surface air and the topsoil. The OTC (60° inclination of the panels, 0.4 m tall and 1.0 m basal diameter) was made of transparent polymethyl methacrylate and placed in the field to achieve year-round warming. The OTC warming method indeed has some limitations (see details in Supplementary Note 5), but has been widely used in remote areas without electricity[46,56,57]. In total, six warming experiments (three thermo-erosion gullies × two areas (thermokarst and non-thermokarst areas)) each with ten replicates were established at the Shaliuhe site. It should be noted that all blocks were laid on vegetated patches rather than on bare soil within the thermokarst landscape (Extended Data Fig. 2f). Despite the inevitable soil translocation after permafrost collapse, topsoils in vegetated patches have retained their original shape due to the protection by mattic epipedon[58,59], which allows more direct comparison between the collapsed areas and non-collapsed areas. Considering that ignoring bare soil within the thermokarst landscape might lead to bias in extrapolation of the thermokarst effect globally, we conducted a supplementary experiment to explore whether and how warming effects on Rs would differ between bare soil and vegetated patches. Our additional measurements showed that there was a similar response of Rs to experimental warming between bare soil

and vegetated patches, indicating no significant influence of ignoring bare soil on the extrapolation (see Supplementary Note 6 for details).

Rs measurements. The Rs and its heterotrophic component were monitored using a Li-8100A Automated Soil CO_2 Flux System (LI-COR Inc.). The trenching method was used to separate Rs components[27,28]. Specifically, we installed two PVC collars (20 cm in diameter) in each plot, one 5-cm-long collar was pushed 3 cm into the soil for measuring Rs, and the other 42-cm-long collar was inserted to a depth of 40 cm for measuring Rh. Given that most roots (~90%) were distributed within 0–40 cm at our study site[13], the 42-cm-long collar was able to block the majority of roots and thus the respiration from roots. To minimize the effects of soil disturbance, PVC collars were installed in June 2018, one year before the first measurement. Rs and its heterotrophic component were measured three times a month during the growing seasons (May to October) in 2019 and 2020. Living plant materials within the collars were removed at least one day before flux measurement to eliminate aboveground plant respiration[60]. All measurements were conducted at 9:00 a.m.–12:00 p.m. local time. During the period of soil CO_2 flux measurement, we did not observe any obvious loosening contact of soils with the inner edges of the collars (Supplementary Fig. 8).

Although the trenching method has been widely used for separation of Rs components[27,28,61], the exclusion of active roots in the deep collars would create an artificial situation without root exudates, which fuel a large share of the microbial respiration. To avoid misleading, we used the concept 'potential heterotrophic respiration (Rhp)' to signal that it was not the actual Rh, but a potential Rh under our specific experimental conditions. Considering this point, the Rhp data obtained in this study were only used to support major findings derived from Rs measurements. At the same time as flux measurement, soil temperature and moisture in the 0–10 cm layer were measured adjacent to collars manually using a TP101 portable thermometer (Shanghai Automation Instrument Factory) and a TDR100 portable soil moisture probe (Spectrum Technologies Inc.), respectively. Additionally, we determined topsoil temperature and moisture inside the collars four times during the experimental period, and observed no significant differences between inside and outside collars (Supplementary Fig. 9).

Determination of vegetation and edaphic properties

Vegetation survey. To characterize the associations between Rs response and plant properties, we determined the normalized difference vegetation index (NDVI), vegetation community composition and plant height during the peak growing season (late July) in 2019. Specifically, we set a 25 × 25 cm² quadrat near each collar, and measured the NDVI using an ADC multi-spectral digital camera (Tetracam). We also counted the number of species, estimated the relative coverage and measured the maximum height of each species in the quadrat. Based on these measurements, we obtained the NDVI, species richness, Shannon index and community-level mean plant height for each plot.

Soil sampling. We collected 60 samples (three thermo-erosion gullies × two areas (thermokarst and non-thermokarst areas) × ten replicates) of topsoil (0–10 cm; organic horizon with SOC larger than 20%; Supplementary Fig. 7) using an auger (3 cm in diameter) adjacent to the PVC collars during the peak growing season in 2019. In each replicate, three soil cores were collected and then mixed into one composite sample. Subsequently, soil samples were sieved through a 2 mm mesh, with the roots and organic debris being manually picked out. Each sample was subdivided into four subsamples. One subsample was immediately frozen in liquid nitrogen (N) and subsequently stored at −80 °C for DNA extraction, one subsample was stored at −20 °C for microbial biomass analysis and incubation experiment, one subsample was kept fresh at 4 °C to determine the inorganic N concentration and the activities of extracellular enzymes, and the remaining part was air-dried and ground for all other analyses. To determine the differences in abiotic and biotic

factors between collapsed and non-collapsed areas, we measured a series of variables such as soil physicochemical properties, mineral protection, substrate quality and microbial properties.

Soil physicochemical and mineral analyses. We determined a number of edaphic variables including soil total C and N concentrations, soil inorganic N (sum of NH_4^+-N and NO_3^--N) and phosphorus concentrations, soil pH, texture, bulk density and the water-filled pore space (see Supplementary Note 7 for details). We also measured the concentration of organically complexed Fe (Fe_p) in the bulk soil. Specifically, Fe_p was extracted using 0.1 M sodium pyrophosphate[62]. The soil solutions were then shaken in the dark and centrifuged to measure the amount of Fe in the supernatants. Fe concentration was determined using an iCAP6300 inductively coupled plasma optical emission spectroscopy (Thermo Scientific).

Substrate quality. Soil substrate quality was analysed on 60 samples using the solid-state ^{13}C nuclear magnetic resonance technique[63]. Specifically, soil samples were treated with 10% hydrofluoric acid repeatedly, rinsed with deionized water and freeze-dried[36]. Approximately 100 mg of the treated soil samples were analysed using an AVANCE NEO 600 MHz spectrometer (Bruker BioSpin), operating at 100.6 MHz, 8 kHz MAS spinning rate, 2 ms contact time and 6 s recycle delay[25]. The spectra were integrated into the following chemical shift regions, and the relative intensities were acquired as the relative abundances of the corresponding C components: alkyl C (0–50 ppm), O-alkyl C (50–110 ppm), aromatic C (110–165 ppm) and carboxylic C (165–220 ppm)[25]. O-alkyl C is generally considered to be more easily decomposed by soil microorganisms, while alkyl C is recalcitrant[25,36]. The alkyl/O-alkyl ratio was then used to represent substrate quality.

Microbial biomass and enzyme activity. Considering the important role of soil microorganisms in mediating the response of Rs to experimental warming, we measured soil microbial biomass and the activities of extracellular enzymes. The contents of microbial biomass C (MBC) and N (MBN) were determined by chloroform fumigation[64,65], with the conversion factors being 0.45 and 0.54, respectively[66,67]. We also assayed the activities of four extracellular hydrolases, β-1,4-glucosidase (BG), β-1,4-*N*-acetyl-glucosaminidase (NAG), leucine aminopeptidase (LAP) and phosphatase (AP) using fluorescence measurements[68], as well as one extracellular oxidase (phenol oxidase) measured by spectrophotometry according to ref. 69 (see details in Supplementary Note 8).

Amplicon sequencing and bioinformatic analyses. The bacterial and fungal communities in the topsoil were determined using amplicon sequencing. Briefly, DNA was extracted from ~0.5 g of fresh soil by the DNeasy PowerSoil Pro Kit (Qiagen), and the concentration and quality of the DNA were analysed using a NanoDrop 2000 spectrophotometer (Thermo Fisher Scientific). Primers 515 F (5′-GTGCCAGCMGCCGC GGTAA-3′)/806 R (5′-GGACTACVSGGGTATCTAAT-3′)[70] and ITS3 (5′-GCATCGATGAAGAACGCAGC-3′)/ITS4 (5′-TCCTCCGCTTATTGAT ATGC-3′)[71] were chosen to amplify the hypervariable V4 region of the bacterial *16S* rRNA gene and the fungal *ITS2* rRNA gene, respectively. The PCR products were purified with the EZNA Gel Extraction Kit (Omega Bio-Tek), and the sequencing library was generated using NEBNext Ultra DNA Library Prep Kit for Illumina (New England Biolabs). Finally, the sequencing library was sequenced by an Illumina Miseq sequencer (Illumina Inc.). Raw reads were quality-filtered and merged using Trimmomatic[72] and FLASH v. 1.2.11 (ref. 73). Merged reads were clustered into operational taxonomic units (OTUs) at 97% identity based on USEARCH (v. 11)[74] after removing chimeras. Bacterial and fungal taxonomy of OTUs were annotated using SILVA v. 123 (ref. 75) and UNITE v. 7.1 (ref. 76), respectively. OTU tables were rarefied at 54,963 for bacteria and 41,219 for fungi, respectively (see Supplementary Note 9 for more details).

Metagenomic sequencing and bioinformatic analysis. Shotgun metagenomic sequencing was used for analysing the topsoil microbial functional genes. Specifically, we performed 2 × 150 bp paired-end sequencing using the Illumina HiSeq 2500 platform. A total of 5.45 billion reads with an average of 13.6 Gbp (s.e.m. = 0.2 Gbp) of sequence data were obtained for each of the 60 samples. Raw sequences were quality-controlled using Trimmomatic (v. 0.39)[72]. The clean data were then de novo assembled (*k*-mer options: *k*-min 35, *k*-max 95, *k*-step 20) using MEGAHIT (v. 1.2.9)[77]. After assembly, scaftigs longer than 500 bp were retained and predicted using Prodigal (v. 2.6.3)[78] to obtain open reading frames (ORFs). The predicted ORFs were dereplicated using MMseqs2 (ref. 79), with the longest ORF used as a representative sequence for each cluster by setting the similarity threshold as 95% and coverage as 90%. Finally, functional genes were annotated by the Kyoto Encyclopedia of Genes and Genomes (KEGG) database[80]. To evaluate the gene abundance, clean reads derived from each sample were mapped to the gene clusters using Bowtie2 (v. 1.0)[81], and counts and lengths of genes and alignments were extracted using SAMtools (v. 1.3.1)[82]. Abundance of genes was normalized to transcripts per million.

Incubation experiment

To validate the generality of the results obtained from the field warming experiments, we collected topsoil (0–10 cm) samples from five additional thermokarst-impacted sites in Ebo, Mole, Reshui, Huashixia and Huanghe (Extended Data Fig. 1) in August 2020. The thermokarst landforms for all sites belong to the thermo-erosion gully (Supplementary Table 1). We established a collapsed plot (10 × 10 m²) inside the gully and a paired control plot in the adjacent undisturbed grassland for each thermokarst-impacted site. In each plot, we sampled five quadrats (1 × 1 m²) at the centre and the four corners. Three soil cores were collected in each quadrat and homogenized as one replicate, with five replicates being ultimately obtained from each plot (n = 5). In total, 50 topsoil samples were collected from the five thermokarst-impacted sites (five thermo-erosion gullies × two plots (collapsed versus non-collapsed plot) × five replicates). All soil samples were sieved through a 2 mm mesh and we manually picked out visible roots.

An incubation experiment was conducted to estimate the temperature sensitivity of soil CO_2 emission (that is, Q_{10}) for the Shaliuhe site and the five additional thermokarst-impacted sites. Samples from all sites were incubated at two temperatures (5 and 15 °C, within the range of mean monthly air temperature across study sites) during a 60-day period. Specifically, 10 g of fresh soil was weighed into a 150 ml airtight amber jar. We adjusted soil moisture to 60% water holding capacity and kept it constant during the incubation by adding demineralized water to the samples. All samples were pre-incubated for seven days at 5 °C to recover them from physical disturbances. The rate of CO_2 release during the next 60 days of incubation was measured every 2–3 days for the first week, every 4–7 days for the next three weeks and every 10 days for the remainder of the period. All incubation jars and three empty jars were flushed using CO_2-free air before each measurement, with the empty jars used as blanks. We collected 10 ml of headspace air after 10 hours of incubation at 5 °C and 15 °C with gas-tight syringes for CO_2 analysis using an EGM-5 infrared gas analyser (PP Systems). Notably, CO_2 dissolution was not considered because this process should be negligible compared with biotic CO_2 release in our acid and organic-matter-rich soils[83,84].

Statistical analyses

Data were processed following four steps. First, we calculated the normalized Rs change and apparent Q_{10} for the field experiments as well as Q_{10} for the laboratory incubation experiment. Specifically, the normalized Rs change was adopted to facilitate comparison of the warming effects between collapsed and non-collapsed areas, that is, the warming-induced changes in Rs were normalized to per unit

temperature change using equation (1) described in the main text. Apparent Q_{10} was calculated based on the seasonal Rs (Supplementary Note 1). The Q_{10} for laboratory incubation was calculated based on the rate of CO_2 release at the two incubation temperatures as follows[34]:

$$Q_{10} = (R_w/R_c)^{[10/(T_w-T_c)]} \qquad (2)$$

where R_w and R_c are the average rates of CO_2 release (mg CO_2-C g^{-1} d^{-1}) at 15 °C (T_w) and 5 °C (T_c), respectively.

Second, linear mixed-effects models were applied to compare the differences of normalized Rs change, apparent Q_{10}, abiotic and biotic factors (vegetation characteristics, edaphic properties, substrate quality and microbial attributes) between collapsed and non-collapsed areas. In the mixed-effects models, collapse status was included as a fixed effect, and plot nested in thermo-erosion gully was treated as a random effect for the field warming experiments. Accordingly, for the incubation experiment, we treated collapse status as a fixed factor and plot as a random factor in the mixed-effects models.

Third, we explored the relationships of the normalized Rs change with various factors (vegetation properties, edaphic properties, substrate quality and the abundance of microbial functional genes) using mixed-effects models. Here, the explanatory variables were included as fixed factors, and plot nested in thermo-erosion gully was treated as a random factor. The normality of the residues of the models was tested, and the data were log-transformed when necessary. The linear mixed-effects models were implemented using the nlme package[85].

Finally, SEM was constructed to elucidate the direct and indirect linkages of the biotic and abiotic factors to the normalized Rs change. Before SEM analysis, we constructed an a priori conceptual model of hypothetical relationships (Supplementary Fig. 5). Specifically, we first chose those variables that exhibited significant changes upon permafrost collapse and also were significantly correlated with the normalized Rs change. Then we hypothesized that (1) soil substrate quality was directly linked to normalized Rs change based on the 'C quality–temperature' hypothesis; (2) microbial functional genes involved in SOM decomposition were directly associated with normalized Rs change because soil microorganisms are carriers of the SOM decomposition process; moreover, microbial functional genes and substrate quality could interact with each other; and (3) soil texture and moisture were linked to normalized Rs change directly via mediating mineral absorption and oxygen diffusion, and indirectly through their effects on substrate quality and microbial functional genes. Considering that variables characterizing substrate quality or microbial functional genes were closely correlated, we performed principal component analysis (PCA) to generate comprehensive metrics to represent each group. The first axis of substrate quality and the weighted mean of the first and second components for microbial functional genes, which explained 77.6% and 86.1% of the variations respectively, were selected for constructing the final model (Supplementary Table 2). The SEM was completed using R packages piecewiseSEM[86] and nlme[85]. All above analyses were also conducted for Rhp. All analyses were conducted in R 4.2.2 (ref. 87).

Data availability
Data used in this study are available from the Figshare data repository https://doi.org/10.6084/m9.figshare.24131997 (ref. 88). The nucleotide sequences generated by metagenome sequencing have been deposited in the NCBI database under BioProject accession number PRJNA1090401.

References

51. Mu, C. et al. The status and stability of permafrost carbon on the Tibetan Plateau. *Earth Sci. Rev.* **211**, 103433 (2020).
52. Gao, T. et al. Accelerating permafrost collapse on the eastern Tibetan Plateau. *Environ. Res. Lett.* **16**, 054023 (2021).
53. IUSS Working Group WRB *World Reference Base for Soil Resources 2014: International Soil Classification System for Naming Soils and Creating Legends for Soil Maps* (FAO, 2014).
54. Yang, Y. et al. Storage, patterns and controls of soil organic carbon in the Tibetan grasslands. *Glob. Change Biol.* **14**, 1592–1599 (2008).
55. Yang, G. et al. Changes in methane flux along a permafrost thaw sequence on the Tibetan Plateau. *Environ. Sci. Technol.* **52**, 1244–1252 (2018).
56. Marion, G. M. et al. Open-top designs for manipulating field temperature in high-latitude ecosystems. *Glob. Change Biol.* **3**, 20–32 (1997).
57. Walker, M. D. et al. Plant community responses to experimental warming across the tundra biome. *Proc. Natl Acad. Sci. USA* **103**, 1342–1346 (2006).
58. Ma, X. et al. Physicochemical properties and micromorphology of degraded alpine meadow soils in the eastern Qinghai–Tibet Plateau. *Catena* **194**, 104649 (2020).
59. Jiang, X. et al. Lateral flow between bald and vegetation patches induces the degradation of alpine meadow in Qinghai–Tibetan Plateau. *Sci. Total Environ.* **751**, 142338 (2021).
60. Mielnick, P. C. & Dugas, W. A. Soil CO_2 flux in a tallgrass prairie. *Soil Biol. Biochem.* **32**, 221–228 (2000).
61. Dorrepaal, E. et al. Carbon respiration from subsurface peat accelerated by climate warming in the subarctic. *Nature* **460**, 616–619 (2009).
62. Gentsch, N. et al. Properties and bioavailability of particulate and mineral-associated organic matter in Arctic permafrost soils, Lower Kolyma region, Russia. *Eur. J. Soil Sci.* **66**, 722–734 (2015).
63. Schmidt, M. W. I., Knicker, H., Hatcher, P. G. & Kogel-Knabner, I. Improvement of ^{13}C and ^{15}N CPMAS NMR spectra of bulk soils, particle size fractions and organic material by treatment with 10% hydrofluoric acid. *Eur. J. Soil Sci.* **48**, 319–328 (1997).
64. Vance, E. D., Brookes, P. C. & Jenkinson, D. S. An extraction method for measuring soil microbial biomass C. *Soil Biol. Biochem.* **19**, 703–707 (1987).
65. Brookes, P. C., Landman, A., Pruden, G. & Jenkinson, D. S. Chloroform fumigation and the release of soil nitrogen: a rapid direct extraction method to measure microbial biomass nitrogen in soil. *Soil Biol. Biochem.* **17**, 837–842 (1985).
66. Tischer, A., Potthast, K. & Hamer, U. Land-use and soil depth affect resource and microbial stoichiometry in a tropical mountain rainforest region of southern Ecuador. *Oecologia* **175**, 375–393 (2014).
67. Joergensen, R. G. The fumigation–extraction method to estimate soil microbial biomass: calibration of the k_{EC} value. *Soil Biol. Biochem.* **28**, 25–31 (1996).
68. German, D. P. et al. Optimization of hydrolytic and oxidative enzyme methods for ecosystem studies. *Soil Biol. Biochem.* **43**, 1387–1397 (2011).
69. Saiya-Cork, K. R., Sinsabaugh, R. L. & Zak, D. R. The effects of long term nitrogen deposition on extracellular enzyme activity in an *Acer saccharum* forest soil. *Soil Biol. Biochem.* **34**, 1309–1315 (2002).
70. Delgado-Baquerizo, M. et al. Changes in belowground biodiversity during ecosystem development. *Proc. Natl Acad. Sci. USA* **116**, 6891–6896 (2019).
71. Yang, T. et al. Soil fungal diversity in natural grasslands of the Tibetan Plateau: associations with plant diversity and productivity. *N. Phytol.* **215**, 756–765 (2017).
72. Bolger, A. M., Lohse, M. & Usadel, B. Trimmomatic: a flexible trimmer for Illumina sequence data. *Bioinformatics* **30**, 2114–2120 (2014).
73. Magoč, T. & Salzberg, S. L. FLASH: fast length adjustment of short reads to improve genome assemblies. *Bioinformatics* **27**, 2957–2963 (2011).

74. Edgar, R. C. Search and clustering orders of magnitude faster than BLAST. *Bioinformatics* **26**, 2460–2461 (2010).

75. Quast, C. et al. The SILVA ribosomal RNA gene database project: improved data processing and web-based tools. *Nucleic Acids Res.* **41**, D590–D596 (2012).

76. Kõljalg, U. et al. Towards a unified paradigm for sequence-based identification of fungi. *Mol. Ecol.* **22**, 5271–5277 (2013).

77. Li, D., Liu, C. M., Luo, R., Sadakane, K. & Lam, T. W. MEGAHIT: an ultra-fast single-node solution for large and complex metagenomics assembly via succinct de Bruijn graph. *Bioinformatics* **31**, 1674–1676 (2015).

78. Hyatt, D. et al. Prodigal: prokaryotic gene recognition and translation initiation site identification. *BMC Bioinform.* **11**, 119 (2010).

79. Steinegger, M. & Söding, J. MMseqs2 enables sensitive protein sequence searching for the analysis of massive data sets. *Nat. Biotechnol.* **35**, 1026–1028 (2017).

80. Kanehisa, M., Sato, Y., Kawashima, M., Furumichi, M. & Tanabe, M. KEGG as a reference resource for gene and protein annotation. *Nucleic Acids Res.* **44**, D457–D462 (2015).

81. Langmead, B. & Salzberg, S. L. Fast gapped-read alignment with Bowtie 2. *Nat. Methods* **9**, 357–359 (2012).

82. Li, H. et al. The sequence alignment/map format and SAMtools. *Bioinformatics* **25**, 2078–2079 (2009).

83. Angert, A. et al. Using O_2 to study the relationships between soil CO_2 efflux and soil respiration. *Biogeosciences* **12**, 2089–2099 (2015).

84. Ma, J., Wang, Z. Y., Stevenson, B. A., Zheng, X. J. & Li, Y. An inorganic CO_2 diffusion and dissolution process explains negative CO_2 fluxes in saline/alkaline soils. *Sci. Rep.* **3**, 2025 (2013).

85. Pinheiro, J., Bates, D., Debroy, S. & Sarkar, D. *nlme: Linear and Nonlinear Mixed Effects Models*. https://svn.r-project.org/R-packages/trunk/nlme (2014).

86. Lefcheck, J. S. piecewiseSEM: piecewise structural equation modelling in R for ecology, evolution, and systematics. *Methods Ecol. Evol.* **7**, 573–579 (2016).

87. R Core Team *R: A Language and Environment for Statistical Computing* (R Foundation for Statistical Computing, 2022).

88. Wang, G. et al. Intensified warming effects on soil respiration upon thermokarst formation. *Figshare* https://doi.org/10.6084/m9.figshare.24131997 (2024).

89. Zou, D. et al. A new map of permafrost distribution on the Tibetan Plateau. *Cryosphere* **11**, 2527–2542 (2017).

Author contributions

Y.Y. conceived the idea. Y.Y. and Y.P. designed the research. G.W., B.W., Y.L., Q.L., J.W. and J.Y. performed the experiments. G.W. and L.C. analysed the data. Y.P., G.W. and Y.Y. wrote the paper with inputs from J.P., B.W.A., P.C., J.S., P.S., D.Z., S.Q., L.K. and Y.S.

Competing interests

The authors declare no competing interests.

Additional information

Extended data is available for this paper at https://doi.org/10.1038/s41561-024-01440-2.

Supplementary information The online version contains supplementary material available at https://doi.org/10.1038/s41561-024-01440-2.

**Correspondence and requests for materials** should be addressed to Yuanhe Yang.

Peer review information *Nature Geoscience* thanks the anonymous reviewers for their contribution to the peer review of this work. Primary Handling Editor: Xujia Jiang, in collaboration with the *Nature Geoscience* team.

**Reprints and permissions information** is available at www.nature.com/reprints.
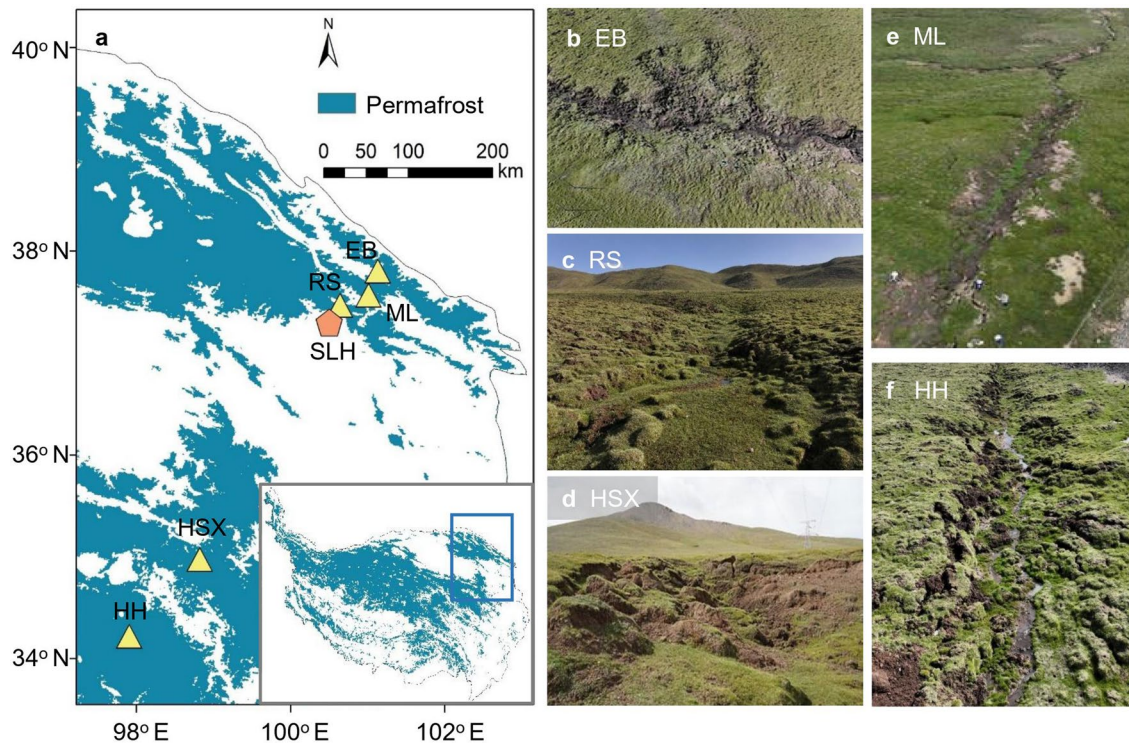
Extended Data Fig. 1 | Locations and landscapes of six thermokarst-impacted sites across the Tibetan Plateau. a, Positions of six study sites shown on the background of permafrost map on the Tibetan Plateau. The pentagon refers to the site where the *in situ* warming experiments were conducted and the triangles denote the locations of regional thermokarst soil sampling. The insert shows regional location on the Tibetan Plateau. **b-f**, Individual features of the thermokarst-impacted sites at EB (**b**), RS (**c**), HSX (**d**), ML (**e**) and HH (**f**). EB, Ebo site; RS, Reshui site; HSX, Huashixia site; ML, Mole site; HH, Huanghe site. The background map of permafrost distribution is from ref. 89. Photograph credit: G.Q. Wang.
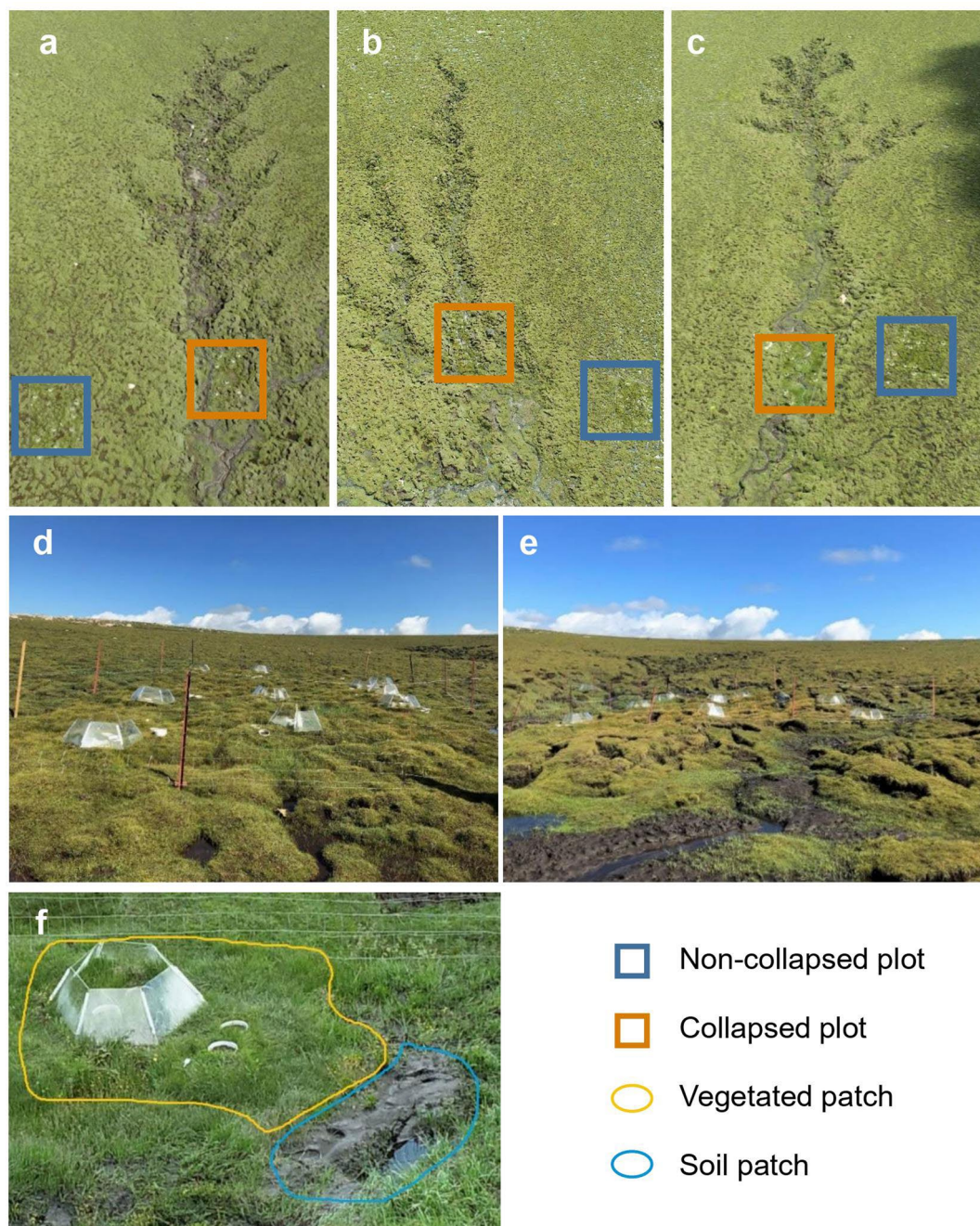
Extended Data Fig. 2 | Landscapes of the three thermo-erosion gullies and views of warming experiments at the Shaliuhe site. a-c, Photographs of the three thermo-erosion gullies at the Shaliuhe site. **d,e**, Overall views of warming experiments in non-collapsed (**d**) and collapsed (**e**) areas from panel (**a**). **f**, A photo showing the warming treatment on the vegetated patch. The open-top chambers were built within the vegetated patches in the collapsed plots, which were formed by the fragmentation of the soil surface upon permafrost collapse. Given that the upper soil was protected by mattic epipedon which had an intensive root network protecting the soil against interference[58,59], these vegetated patches maintained their original soil structure, despite the translocation of the exposed soil upon permafrost collapse[13]. Photograph credit: G.Q. Wang.
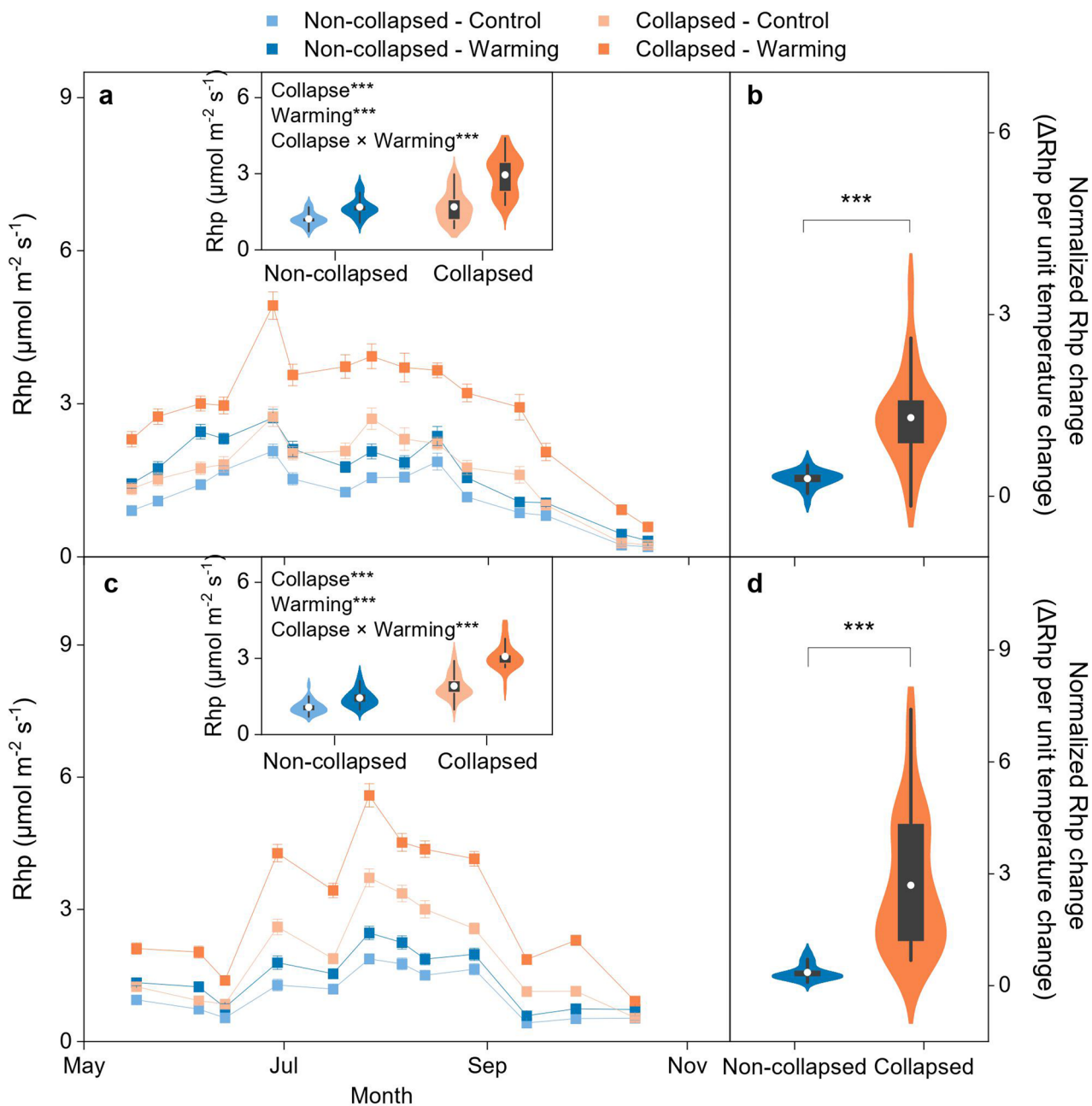
Extended Data Fig. 3 | Responses of potential heterotrophic respiration (Rhp) to permafrost collapse and experimental warming at the Shaliuhe site. a,c, Seasonal dynamics and averages of Rhp during the growing seasons in 2019 (**a**) and 2020 (**c**). Data are presented with mean values ± s.e.m. (*n* = 30). Inserts show effects of permafrost collapse, experimental warming and their interactions on seasonal averages of Rhp. **b,d**, Normalized Rhp change between collapsed and non-collapsed areas in 2019 (**b**) and 2020 (**d**). The ends of the boxes represent the 25th and 75th percentiles, and the whiskers refer to the 10th and 90th quartiles. The white dot in each box shows the average (*n* = 30). These comparisons were analyzed based on linear mixed-effects models with one-sided *F* tests. ***, *P* < 0.001.
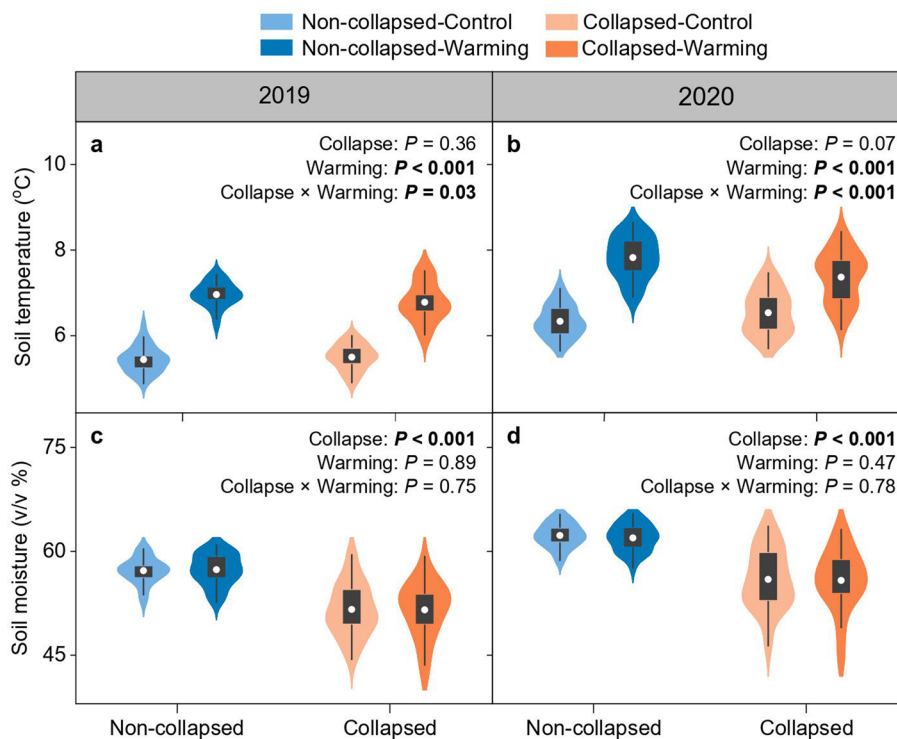
Extended Data Fig. 4 | Responses of topsoil (0-10 cm) temperature and moisture to permafrost collapse and experimental warming at the Shaliuhe site. a,b, Effects of permafrost collapse, experimental warming and their interactions on soil temperature in 2019 (**a**) and 2020 (**b**). **c,d**, Effects of permafrost collapse, experimental warming and their interactions on soil moisture in 2019 (**c**) and 2020 (**d**). The ends of the boxes represent the 25th and 75th percentiles, and the whiskers refer to the 10th and 90th quartiles. The white dot in each box represents the average (n = 30). Both soil temperature and moisture were measured manually during Rs monitoring. These comparisons were analyzed based on linear mixed-effects models with one-sided F tests.
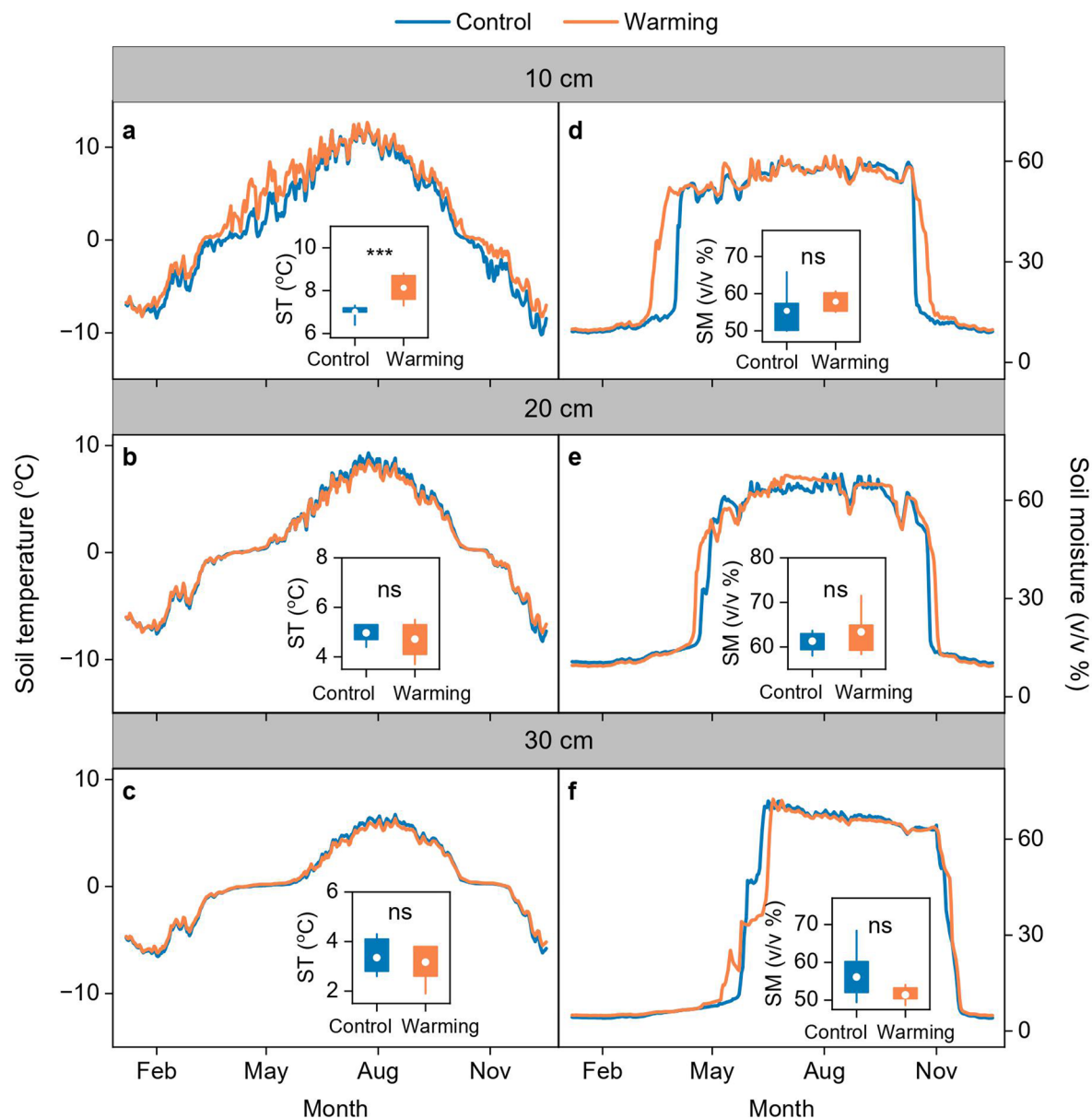
Extended Data Fig. 5 | Effects of experimental warming on temperature and moisture in different soil layers of non-collapsed areas at the Shaliuhe site. a-c, Daily soil temperature at depth of 10 cm (**a**), 20 cm (**b**) and 30 cm (**c**) from January to December. **d-f**, Daily soil moisture at depth of 10 cm (**d**), 20 cm (**e**) and 30 cm (**f**) from January to December. The inserts show the averages of soil temperature and moisture across the growing season (May - October).

ST, soil temperature; SM, soil moisture. The ends of the boxes represent the 25th and 75th percentiles, and whiskers refer to the 10th and 90th quartiles. The white dot in each box represents the average. Significant differences between warming and control plots were determined based on two-sided *t* tests. ns, non-significant; ***, *P* < 0.001. Both soil temperature and moisture were measured by EM50 data loggers (Decagon Devices, Washington, USA) in 2019.
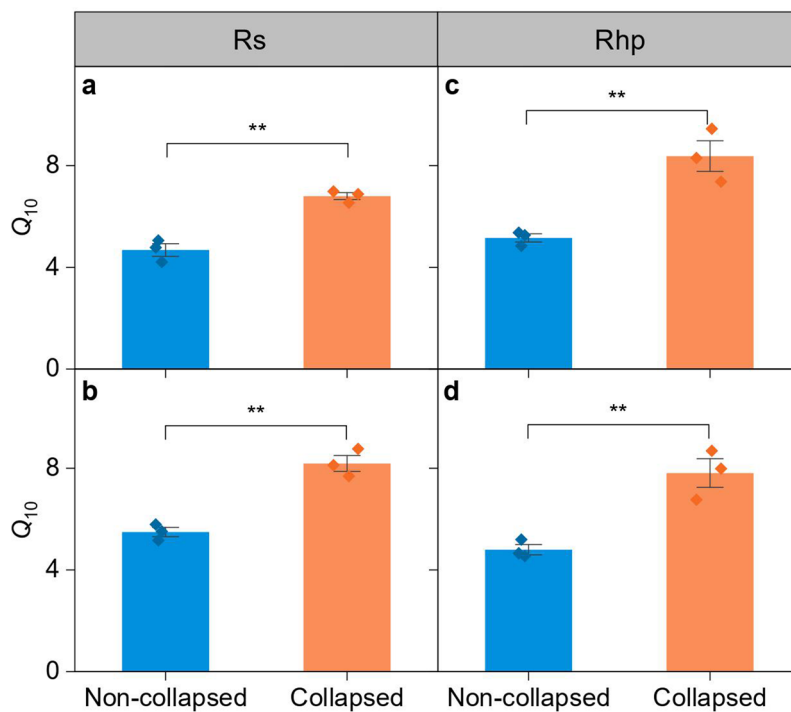
Extended Data Fig. 6 | Comparisons of apparent temperature sensitivity (Q_{10}) of soil respiration (Rs) and potential heterotrophic respiration (Rhp) between collapsed and non-collapsed areas at the Shaliuhe site. a,b, Apparent Q_{10} of Rs during the growing season in 2019 (**a**) and 2020 (**b**). **c,d,** Apparent Q_{10} of Rhp during the growing season in 2019 (**c**) and 2020 (**d**). Apparent Q_{10} was estimated for each gully by fitting the seasonal observations of soil CO_2 flux and soil temperature in the top 10 cm (see Supplementary Note 1 for detailed calculation). Data are presented with mean values ± s.e.m. ($n = 3$). Significant differences between collapsed and non-collapsed areas were determined based on linear mixed-effects model with one-sided F tests. **, $P < 0.01$.
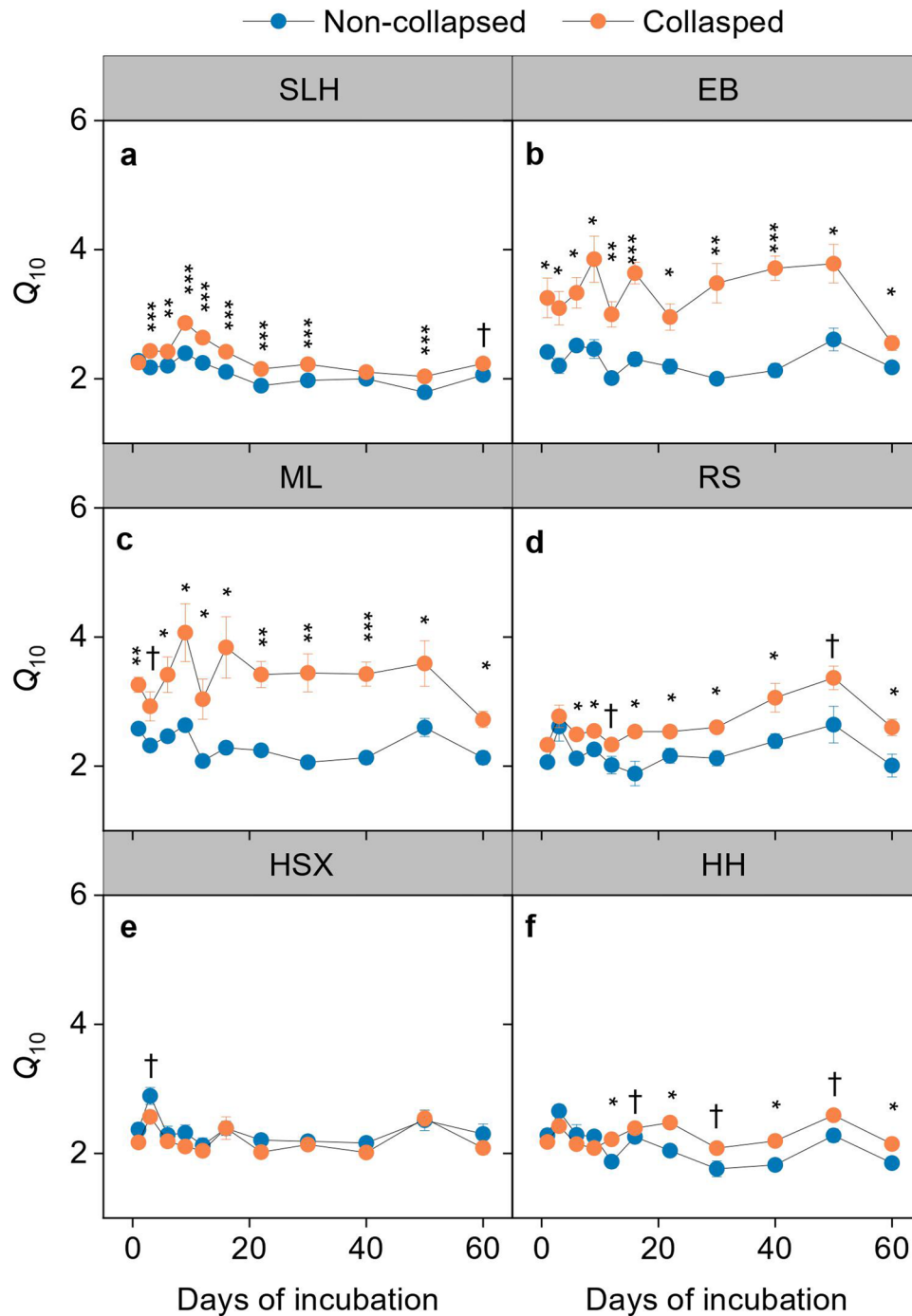
Extended Data Fig. 7 | Temperature sensitivity (Q_{10}) estimated on each measurement occasion during the 60-day laboratory incubation for the six sampling sites. a, Q_{10} between collapsed and non-collapsed areas at the Shaliuhe site. Samples (n = 30) were collected from three thermo-erosion gullies in 2020. **b-f,** Q_{10} between collapsed and non-collapsed areas for the five additional sites.

Samples (n = 5) were collected in 2020. SLH, Shaliuhe site; EB, Ebo site; ML, Mole site; RS, Reshui site; HSX, Huashixia site; HH, Huanghe site. Data are presented with mean values ± s.e.m. Significant differences between collapsed and non-collapsed areas were determined based on linear mixed-effects models. †, $P < 0.1$; *, $P < 0.05$; **, $P < 0.01$; ***, $P < 0.001$. Samples were collected and analyzed in 2020.
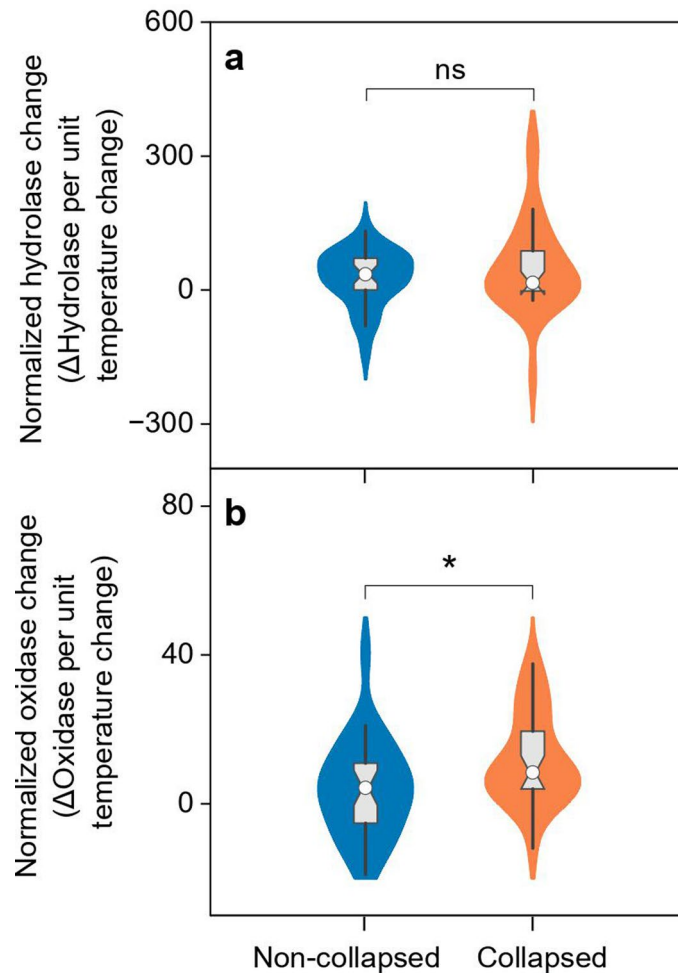
Extended Data Fig. 8 | Comparison of normalized changes in topsoil (0-10 cm) enzyme activities between collapsed and non-collapsed areas at the Shaliuhe site. a,b, Normalized changes in the hydrolase (**a**) and oxidase (**b**) activities. Normalized changes of enzyme activities (ΔEnzyme per temperature change = $(En_{Warming} - En_{Control})/(T_{Warming} - T_{Control})$, where $En_{Warming}$ and $En_{Control}$ are soil enzyme activity (nmol g^{-1} h^{-1}) in the warmed and control plots, and $T_{Warming}$ and $T_{Control}$ are temperature (°C) in the warmed and control plots, respectively) were calculated in collapsed and non-collapsed areas, and weighted by the temperature difference between the warming and control treatments ($T_{Warming} - T_{Control}$) to eliminate the difference of warming effects between collapsed and non-collapsed areas. The ends of the boxes represent the 25th and 75th percentiles, and the whiskers refer to the 10th and 90th quartiles. The white dot in each box shows the average (n = 30). These comparisons were analyzed based on linear mixed-effects models with one-sided F tests. ns, non-significant; *, P < 0.05. Samples were collected from the three thermo-erosion gullies in 2019.
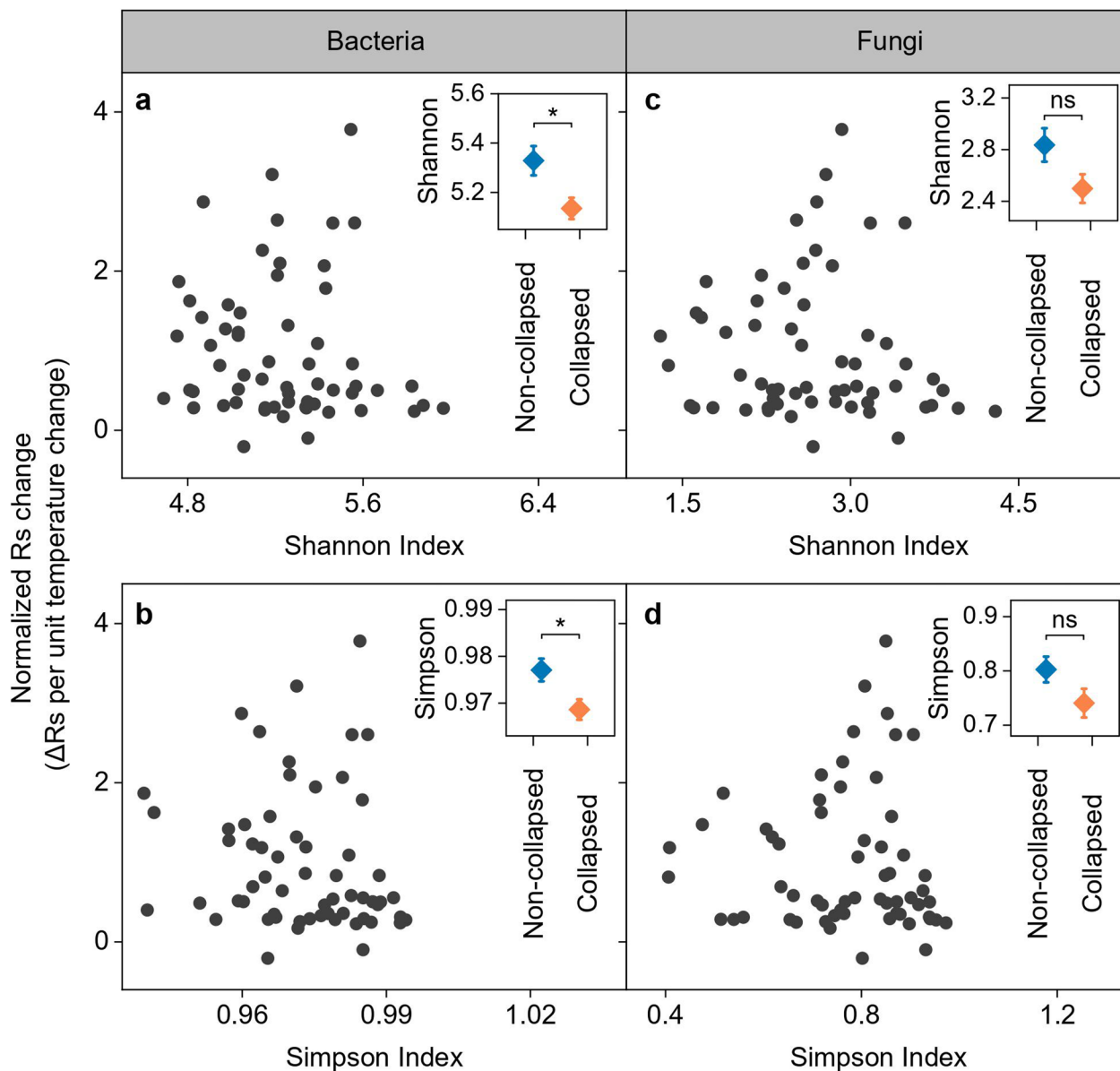
Extended Data Fig. 9 | Thermokarst-induced differences in topsoil (0-10 cm) microbial diversity and their relationships with the normalized soil respiration (Rs) change at the Shaliuhe site. a-d, Relationships of normalized Rs change with Shannon and Simpson indices for bacterial (**a**, **b**) and fungal (**c**, **d**) communities. The inserts denote differences in Shannon and Simpson indices upon permafrost collapse. Data are presented with mean values ± s.e.m. (n = 30). Significant differences between collapsed and non-collapsed areas were determined based on linear mixed-effects models with one-sided F tests. ns, non-significant; *, $P < 0.05$. Samples were collected from the three thermo-erosion gullies in 2019.
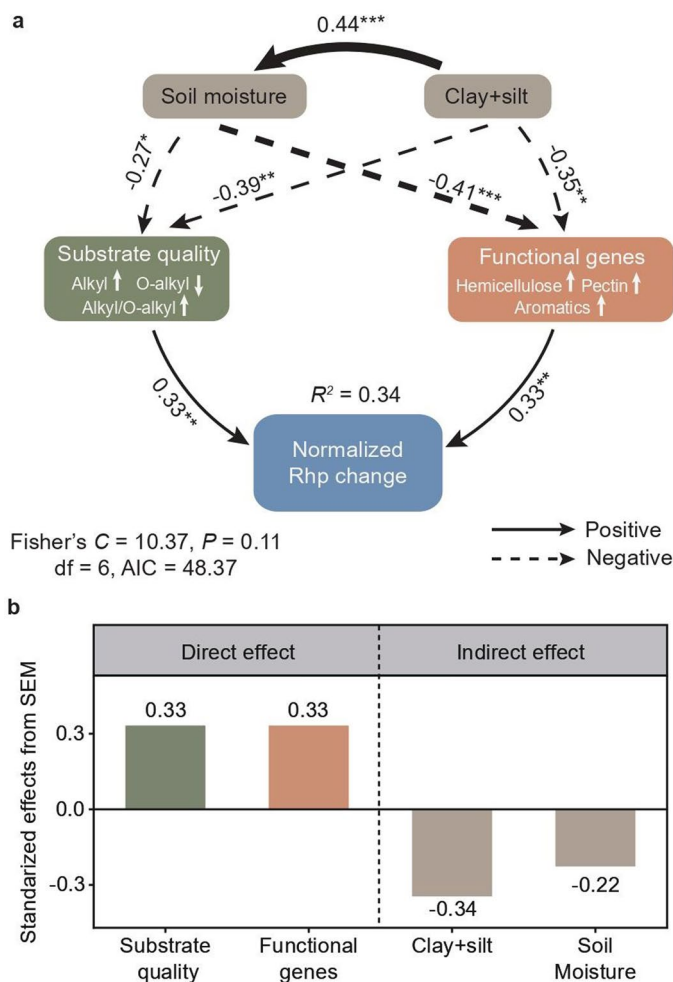
Extended Data Fig. 10 | Effects of abiotic and biotic factors on the normalized potential heterotrophic respiration (Rhp) change. a, Structural equation model (SEM) of the direct and indirect pathways that affect the normalized Rhp change. **b**, Standardized direct effects of substrate quality and the abundances of microbial functional genes and the indirect effects of edaphic variables (clay+silt and soil moisture) on the normalized Rhp change. Solid and dotted arrows represent positive and negative relationships, respectively. Arrow width is proportional to the strength of the relationship. The numbers adjacent to the arrows denote standardized path coefficients. Substrate quality is the first component from the principal component analysis (PCA) conducted with the factors listed in the rectangles, with "↑" and "↓" indicating positive and negative correlations between the factors and the first component, respectively. Microbial functional genes represent the weighted average of the first and second components from the PCA of the factors in the rectangle, with "↑" indicating a positive correlation between the factors and the weighted average of the first and second components. *, $P < 0.05$; **, $P < 0.01$; ***, $P < 0.001$. AIC, Akaike information criterion.